AGU PUBLICATIONS

JGR

Journal of Geophysical Research: Solid Earth

RESEARCH ARTICLE
10.1002/2016JB013191

Mass discharge rate retrieval combining weather radar and thermal camera observations

Gianfranco Vulpiani[1], Maurizio Ripepe[2], and Sebastien Valade[2]

[1]Department of Civil Protection, Presidency of the Council of Ministers, Rome, Italy, [2]Department of Earth Science, University of Florence, Florence, Italy

Key Points:
- A robust approach to derive ash concentration and mean ash diameter from weather radar observations at C and X band is proposed
- Thermal camera imageries are used to derive the exit velocity of the volcanic plume
- Near-vent concentration and mean ash diameter estimates are combined with the exit velocity to compute the mass discharge rate

Correspondence to:
G. Vulpiani,
gianfranco.vulpiani@protezionecivile.it

Citation:
Vulpiani, G., M. Ripepe, and S. Valade (2016), Mass discharge rate retrieval combining weather radar and thermal camera observations, *J. Geophys. Res. Solid Earth*, *121*, doi:10.1002/2016JB013191.

Received 19 MAY 2016
Accepted 1 AUG 2016
Accepted article online 4 AUG 2016

Abstract The mass discharge rate is a key parameter for initializing volcanic ash dispersal models. Commonly used empirical approaches derive the discharge rate by the plume height as estimated by remote sensors. A novel approach based on the combination of weather radar observations and thermal camera imagery is presented here. It is based on radar ash concentration estimation and the retrieval of the vertical exit velocities of the explosive cloud using thermal camera measurements. The applied radar retrieval methodology is taken from a revision of previously presented work. Based on the analysis of four eruption events of the Mount Etna volcano (Sicily, Italy) that occurred in December 2015, the proposed methodology is tested using observations collected by three radar systems (at C and X band) operated by the Italian Department of Civil Protection. The total erupted mass was estimated to be about $9 \cdot 10^9$ kg and $2.4 \cdot 10^9$ kg for the first and second events, respectively, while it was about $1.2 \cdot 10^9$ kg for both the last two episodes. The comparison with empirical approaches based on radar-retrieved plume height shows a reasonably good agreement. Additionally, the comparative analysis of the polarimetric radar measurements provides interesting information on the vertical structure of the ash plume, including the size of the eruption column and the height of the gas thrust region.

1. Introduction

The detection and quantitative retrieval of ash clouds is of significant interest due to the environmental, climatic, and socioeconomic effects of ash fallout [*Cadle et al.*, 1979] which might cause hardship and damages in areas surrounding volcanoes, representing a serious hazard to aircrafts [*Casadeval*, 1994]. Real-time monitoring of such phenomena is crucial for this reason and for initializing ash dispersion models. Ground-based and spaceborne remote sensing observations provide essential information for scientific and operational applications [*Rose et al.*, 2000]. Satellite visible-infrared radiometric observations from geostationary platforms are usually exploited for long-range trajectory tracking and for measuring low-level eruptions [*Rose et al.*, 2000]. Their imagery is available every 10–30 min and suffers from a relatively poor spatial resolution. Moreover, the field of view of geostationary radiometric measurements may be blocked by water and ice clouds at higher levels and the observations' overall utility is reduced at night. Ground-based microwave weather radars may represent an important tool for detecting and, to a certain extent, mitigating the hazards presented by ash clouds [*Maki et al.*, 2001; *Marzano et al.*, 2006a]. The possibility of monitoring in all weather conditions at a fairly high spatial resolution (less than a few hundred meters) and every few minutes after the eruption is the major advantage of using ground-based microwave radar systems [*Harris and Rose*, 1983; *Marzano et al.*, 2006a]. Ground-based weather radar systems can also provide data for estimating the ash volume, total mass, and height of eruption clouds. Previous methodological studies have investigated the possibility of using ground-based single-polarization radar system for the remote sensing of volcanic ash cloud [*Marzano et al.*, 2006a, 2006b]. A microphysical characterization of volcanic ash was carried out in terms of dielectric properties, size distribution (i.e., Gamma or Weibull functions), and terminal fall speed, assuming spherically shaped particles [*Marzano et al.*, 2006a]. A prototype of a volcanic ash radar retrieval (VARR) algorithm for single-polarization systems was proposed by *Marzano et al.* [2006b] and applied to S, C, and X band weather radar data volumes [*Marzano et al.*, 2010a, 2010b, 2013]. The potential benefit derived from the use of dual-polarization radar systems at X band was first tested by *Maki et al.* [2001]. Next, *Marzano et al.* [2012] extended the VARR approach, named VARR-PX (VARR polarimetric at X band), for X band radar polarimetric retrieval of volcanic ash clouds from measured dual-polarization observations. *Montopoli et al.* [2014] found that the use of polarimetric radar observations improved the data quality control, analysis,

and interpretation. Recently, the synergistic use of complementary remote sensing observations (e.g., infrared (IR) and microwave (MW) data collected by radiometers on board satellite platforms, ground-based radar measurements, and thermal camera imagery) was exploited to derive volcanic ash plume height, thickness, and total mass [*Corradini et al.*, 2015].

Despite its elegant mathematical framework, the VARR methodology has shown some limitations once applied in operational contexts. Indeed, anomalies in the retrieved concentration field (e.g., high concentration peaks uncorrelated with reflectivity cores) were shown in *Vulpiani et al.* [2011], *Marzano et al.* [2013], and *Montopoli et al.* [2014] but attributed to high concentrations of small particles. More realistically, the cause of such problems is here attributed to the retrieval algorithm scheme that was conceived beginning from unrealistic simulations derived by nonphysical distribution of the particle size parameters. In the present work, the estimation methodology was revised according to new scattering simulations. Furthermore, because quantitative estimation of the erupted materials in the proximity of the volcano's vent is crucial for initializing transportation models, a novel approach combining radar and thermal camera observations to estimate the mass discharge rate (MDR) is presented here. Four eruption events of the Mount Etna volcano (Sicily, Italy) that occurred in December 2015 were analyzed. The paper is organized as follows: Section 2 describes the fundaments of radar remote sensing of volcanic ash (radar volcanology), and section 3 presents the proposed methodology for the MDR estimation. The adopted approach to estimating exit velocity is summarized in section 4. The data set is presented in section 5, the results are discussed in section 6, and conclusions are presented in section 7.

2. Background

2.1. Moments of the Particle Size Distribution

The particle size distribution (PSD) describes the particle size occurrence per unit volume (e.g., the unit is in m^{-3} mm^{-1}). The ash PSD, assumed to follow a scaled Gamma distribution [*Marzano et al.*, 2006a], is indicated by $N(D)$, where D (mm) is the equivolume-sphere particle diameter.

From a knowledge of PSDs and their shape and composition, some meaningful parameters can be introduced. Assuming that the ash particles are spherical or, at least, sphere equivalent, the ash particle mass m_a (g) can be written as

$$m_a(D) = \frac{\pi}{6}\rho_a D^3 \tag{1}$$

where ρ_a (g cm^{-3}) is the ash density, assumed to be independent of diameter D (here expressed in cm). The nth order moment $E[D^n]$ of $N(D)$ is

$$E[D^n] = \int_{D_{\min}}^{D_{\max}} D^n N(D)\mathrm{d}D \tag{2}$$

where $D_{\min}$ and $D_{\max}$ are the minimum and maximum diameters, respectively.

Consequently, the mass concentration within a given atmospheric volume C_a (g m^{-3}) and the mean diameter are given by

$$C_a \equiv \int_{D_{\min}}^{D_{\max}} m_a(D)N(D)\mathrm{d}D = \frac{\pi}{6}\rho_a E[D^3] \tag{3}$$

$$D_m \equiv \frac{\int_{D_{\min}}^{D_{\max}} DN(D)}{\int_{D_{\min}}^{D_{\max}} N(D)}\mathrm{d}D = E[D]/E[D^0] = E[D]/N \tag{4}$$

where N is the total number of particles, $E[D^3]$ and $E[D]$ are, respectively, the third- and first-order moments of the assumed normalized Gamma particle size distribution that according to *Marzano et al.* [2006a] assumes the form

$$N(D) = N_G \left(\frac{D}{D_m}\right)^{\mu} \exp\left[-(\mu+1)\frac{D}{D_m}\right] \tag{5}$$

with $N_G = \frac{6}{\pi\rho_a}\frac{(\mu+1)^{(4+\mu)}C_a D_m^{-4}}{(3+\mu)}$.

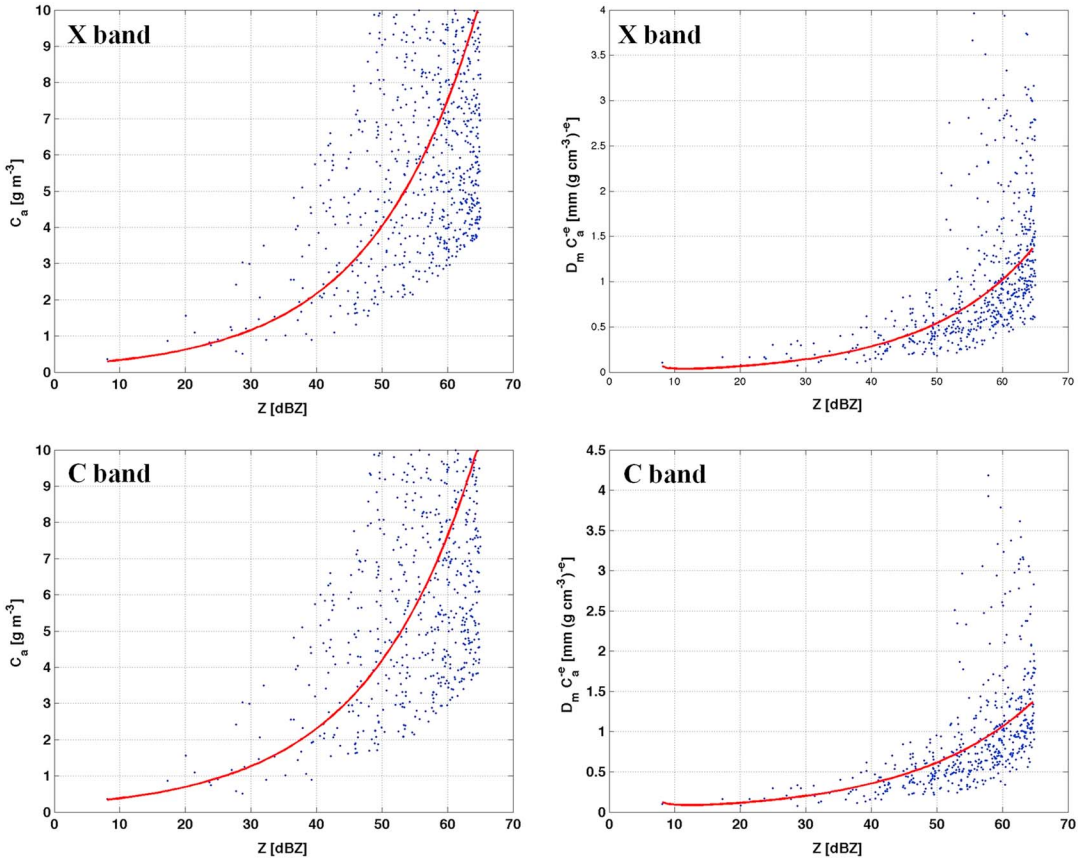

Figure 1. Scatterplot of C_a versus Z and D_m normalized by C_a^e versus Z at (top row) X and (bottom row) C band as obtained from scattering simulations. The fitting curve is depicted in red color.

The radar reflectivity factor Z (mm^6 m^{-3}) can be expressed in the Rayleigh approximation as a sixth-order moment of $N(D)$

$$Z = \int_{D_1}^{D_2} D^6 N_a(D) \mathrm{d}D = E[D^6] \tag{6}$$

From (3) and (5), it is possible to deduce that $\frac{C_a}{Z} \propto \frac{m_3}{m_6}$. Consequently, a power law is expected to relate C_a and Z

$$C_a = aZ^b \tag{7}$$

where Z is expressed in linear units.

In the Rayleigh regime, it can be shown that D_m can be expressed in terms of Z and C_a as follows [*Marzano et al.*, 2006a]

$$D_m = \sqrt[3]{\frac{Z\rho_a}{f_Z C_a}} \tag{8}$$

with

$$f_Z = \frac{610^6 \Gamma(\mu+7)}{\pi(\mu+1)^3 \Gamma(\mu+3)} \tag{9}$$

where Γ is the gamma function and μ the shape parameter of the assumed Gamma size distribution. Consequently, a general power law of the form

$$D_m = cZ^d C_a^e \tag{10}$$

can be retrieved from scattering simulations.

Table 1. Regression Coefficients Relating Ash Concentration and Radar Reflectivity Factor for the Case of Unitary Ash Particle Density

Band	a_0	b
C	0.21	0.26
X	0.18	0.27

Before computing the ash concentration and mean diameter through (7) and (10), the reflectivity factor must be rescaled into the ash-equivalent reflectivity (Z (dBZ) = Z_m + 3.77) because the measured reflectivity Z_m is calibrated assuming the dielectric factor of water [*Marzano et al.*, 2006a].

2.2. Scattering Simulations

In previous works [*Marzano et al.*, 2006a, 2006b], an inversion methodology was developed using scattering simulations of the radar observables obtained applying the T matrix solution technique [*Mishchenko*, 2000; *Vulpiani*, 2010] beginning with some synthetic microphysical scenarios.

Adopting a Gamma particle size distribution as in (5), C_a and D_m were randomly generated following a normal distribution with predefined mean and standard deviation. Nine data sets, corresponding to three eruption regimes (light, moderate, and intense) for each of the three diameter classes (fine, coarse, and lapilli) were generated and then used to compute the corresponding radar observables. Next, the number of microphysical scenarios was extended by discriminating small from large lapilli [*Marzano et al.*, 2012].

The developed retrieval algorithm (named VARR) was based on the application of inversion relationships specific for each of the predefined microphysical scenarios, as preliminarily identified through a Bayesian classification methodology. The limit of this approach relies on a pronounced and unrealistic clustering of the microphysical scenarios due to the assumption of (low-dispersed) normal distribution of C_a and D_m. Indeed, the corresponding radar observables, such as the reflectivity factor, are unavoidably clusterized as well. Consequently, the overall inversion algorithm causes "jump discontinuities" which eventually sharpen by misclassification.

To remove this limit, a continuous microphysical scenario was considered assuming uniformly distributed PSD parameters. C_a and D_m were assumed to vary within the following domains: $0 < C_a \leq 10$ g m^{-3} and $10^{-4} \leq D \leq 20$ mm. The maximum particle diameter is limited by the computational efficiency of the adopted numerical scattering code.

Regarding the particle shape, axis ratio, composition, and resulting dielectric constant, the parameterization proposed in [*Marzano et al.*, 2012] was assumed here. More specifically, the particles were assumed to be oblate spheroids with an axis ratio depending on the diameter through a linear model derived by the data reported in *Riley et al.* [2003]. Based on the measurements reported in *Adams et al.* [1996], the dielectric constant model was assumed to depend linearly on the SiO2 content that was randomly varied between 50% and 75%. Air intrusion between 0% and 30% was also considered through the Maxwell-Garnet mixing formula. The particles were assumed to follow a tumbling motion.

Figure 1 shows the simulated C_a and D_m normalized by C_a^e as a function of Z for both X (top row) and C band (bottom row). Resonance scattering effects are noticeable for $Z > 50$ dBZ. To avoid unrealistic simulations, the data set was filtered based on a 65 dBZ thresholding on Z.

Based on a regression analysis, the parameters of (7) and (10) were determined for C and X band (see Tables 1 and 2).

To adapt (7) to any specific volcanological scenario, the multiplicative coefficient a is factorized as $a = \frac{\rho_a}{\rho_0} a_0$, a_0 corresponding to the case of *unitary* density ($\rho_0 = 1$ g cm^{-3}). In this work it was assumed $\rho_a = 1.5$ g cm^{-3}.

Table 2. Regression Coefficients Relating Mean Diameter to Ash Concentration and Radar Reflectivity Factor

Band	c	d	e
C	0.0906	0.266	−0.260
X	0.0585	0.311	−0.313

3. Retrieval of Mass Discharge Rate

The mass discharge rate (MDR) is a crucial parameter for predicting the dynamics of volcanic ash clouds. Indirect approaches are typically used to derive it; e.g., the empirical relation provided by *Mastin et al.* [2009], relating the plume top height to MDR, is currently used by the Volcanic Ash Advisory Centre (VAAC). In this perspective, the plume top height can be estimated by remote sensing observations, e.g., visible camera, radiometer on board of satellite platform, ground-based weather radars, or a combination of the above [*Corradini et al.*, 2015]. Recently, *Mereu et al.* [2015] proposed a complex approach to deriving the MDR from radar observations aloft by applying the continuity equation to the ash cloud. Such a procedure can be used under several simplifications and assumptions. In the present work, it is shown that the MDR can be estimated by combining radar observations as close as possible to the volcano vent and thermal camera estimation of the upward velocity (w^{up}). Neglecting wind-drift effects within the gas thrust region, it is assumed that the ash vertical motion is mainly determined by the balance between gas pressure, gravity, and aerodynamic stress. In the proximity of the volcano vent, the differential of mass per unit area flowing in a unit time interval (kg m^{-2} s^{-1}) can be written as

$$dj_m = \vec{w} \cdot \hat{n} dC_a = w \cos(\alpha) dC_a \tag{11}$$

where $\hat{n}$ is the unit vector perpendicular to the unit area tilted by α from the vertical and dC_a is expressed in kg m^{-3}. $\vec{w}$ is the vertical velocity resulting from upward and downward motion $w = w^{up} - w^{down}$.

The downward motion is modeled, according to *Steinberg and Babenko* [1978], through a power law relating the settling velocity to the particle diameter ($w^{down} = a_v D^{b_v}$) where a_v depends on the drag coefficient C_d and the particle and fluid density (ρ_a and ρ_{fluid}, respectively), whereas $b_v = 0.5$. Assuming that $C_d = 0.5$ and $\rho_{fluid} = 10$ kg m^{-3}, we obtain $a_v = 62.6$ m$^{1-b_v}$ s^{-1}.

Taking the differential of (3) and using (1), (11) becomes

$$dj_m = \cos(\alpha) \frac{\pi}{6} \rho_a w D^3 N(D) \mathrm{d}D \tag{12}$$

where ρ_a and D are expressed here in kg m^{-3} and D in meters, respectively. Integrating (12) and making w explicit, we get

$$j_m = \cos(\alpha) \int_{D_{min}}^{D_{max}} \frac{\pi}{6} \rho_a \left[w^{up} - w^{down} \right] D^3 N(D) \mathrm{d}D = \cos(\alpha) \int_{D_{min}}^{D_{max}} \frac{\pi}{6} \rho_a \left[w^{up} - a_v D^{b_v} \right] D^3 N(D) \mathrm{d}D \tag{13}$$

Assuming that w^{up} is independent of particle size, (13) becomes

$$j_m = \cos(\alpha) \left[w^{up} C_a - \frac{\pi}{6} a_v \rho_a m_{3+b_v} \right] \tag{14}$$

$E[D^{3+b_v}]$ being the $(3 + b_v)$-order moment of the PSD that after some mathematical manipulation based on the property of the Gamma function in (5), can be written as

$$E[D^{3+b_v}] = \frac{6}{\pi \rho_a} \frac{\Gamma(4 + b_v + \mu)}{(\mu + 1)^{b_v} (3 + \mu)!} C_a D_m^{b_v} \tag{15}$$

The assumption regarding w^{up} is valid as long as the proximity of the volcano vent is considered, since w^{up} is mainly related to gas pressure at that location.

Based on (15), (14) becomes

$$j_m = \cos(\alpha) C_a \left[w^{up} - \frac{\Gamma(4 + b_v + \mu)}{(\mu + 1)^{b_v} (3 + \mu)!} a_v D_m^{b_v} \right] \tag{16}$$

where C_a and D_m have to be expressed in kg m^{-3} and meters, respectively.

Starting from (16), retrieving flux density j_m from radar observations is proposed using (7) and (10) in addition to the estimate of w^{up} from thermal camera imagery [*Delle Donne and Ripepe*, 2012] (see section 4 for details).

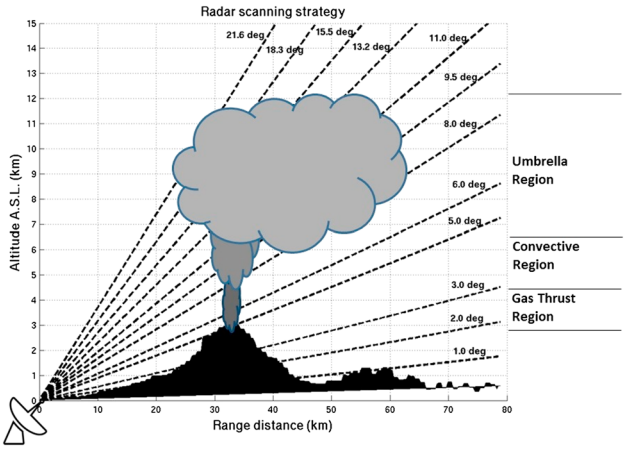

Figure 2. Schematic illustration of the radar scanning geometry in terms of range-height plot adopted for the X band system located in Catania (Sicily, Italy).

For a given radar observation in the native polar coordinates, (16) becomes

$$j_m(r,\theta,\phi) = \cos(\theta) C_a \left[w^{\text{up}} - \frac{\Gamma\left(4 + b_v + \mu\right)}{(\mu+1)^{b_v}(3+\mu)!} a_v D_m(r,\phi,\theta)^{b_v} \right] \tag{17}$$

where $\theta \equiv \alpha$. Because the dependency of (17) on μ is relatively weak, it is assumed that $\mu = 1$.

Finally, the mass discharge rate can be obtained from (17) by computing the surface integral over the lowest unshielded radar tilt ($\theta = \theta_L$) crossing the ash cloud (see Figure 2)

$$\text{MDR} = \int \int j_m(r, \theta_L, \phi) r \text{d}r\text{d}\phi \tag{18}$$

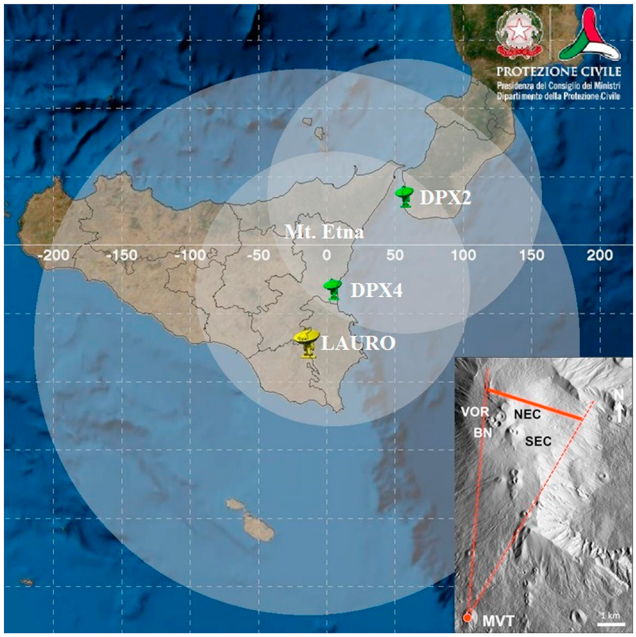

Figure 3. Map showing the location of the radar systems considered here with respect to the Etna volcano. The DPX4 and DPX2 systems are located within the Catania and Reggio Calabria airports, respectively. The LAURO radar system is located on Mount Lauro (Buccheri, Syracuse). The embedded image shows the thermal camera position and the corresponding field of view with respect to the Etna craters, named Voragine crater (VOR), Bocca Nuova crater (BN), northeast crater (NEC) and southeast crater (SEC).

Alternatively, the MDR can be computed after the resampling of the radar observations in Cartesian grid. This is the approach followed in the present study in order to combine the observations collected by the available network of radar systems (depicted in Figure 3). The proposed methodology is named hereinafter near-source radar algorithm (NSR) to emphasize that the lowest available observations are used to compute the MDR.

4. Measuring Exit Velocity

The exit velocity of the volcanic plume was calculated using thermal imagery collected by the thermal camera located on Mount Vetore about 6.8 km south of the active vents at an altitude of about 1800 m above sea level (asl). The image embedded in Figure 3 shows the camera position and the corresponding field of view with respect to the volcano craters. The thermal camera is an FLIR A655sc microbolometric camera, recoding radiometric images at 0.5 frames per second that are then radio-transmitted in real time to the acquisition center in Nicolosi, about 9 km distant. The camera has a 25 × 18.8° angle of view with optical lens of 9.2 mm and a maximum thermal resolution of 0.1°C in the 7.5–13μm wavelength interval. A global positioning system (GPS) time stamp on each frame provides the precise time information for each frame. The camera has a focal plane resolution of 640 × 480 pixels, providing a field of view of the thermal frame 3 km wide by 2.3 km high. Given the camera inclination angle of 18.5°, the field of view above the eruptive vent reduces to approximately 2200 m; that is, 5500 m asl (see Figure 4).

The thermal imagery was processed to measure the volcanic ash plume upward velocities. This was realized by converting thermal pixels in meters and by tracking the vertical propagation of the thermal anomalies related to volcanic plumes in successive frames. The adopted processing was based on the thermal decomposition method of single images as described in detail in *Delle Donne and Ripepe* [2012]. In summary, the thermal images $I_t(t,x,y)$ were converted into binary images $I_b(t,x,y)$ according to the following formulas:

$$I_b(t,x,y) = \begin{cases} 1, & I_t(t,x,y) > T_{\text{bcg}} \\ 0, & I_t(t,x,y) \le T_{\text{bcg}} \end{cases} \tag{19}$$

where T_{bcg} is the ambient background temperature. For each frame I_t, the distribution of pixels (x,y) characterized by temperatures higher than the background T_{bcg}, related to the hot volcanic material (pyroclasts, juvenile ash, etc.), was obtained. The high-temperature pixel distribution in the vertical, V_d, and horizontal, H_d, axes was retrieved by adding all the pixels I_b along the same row and for each column of the image:

$$V_d(t,x) = \sum_{y=1}^{y=Y} I_b(t,x,y) \tag{20}$$

$$H_d(t,x) = \sum_{x=1}^{x=X} I_b(t,x,y) \tag{21}$$

where X and Y stand for the horizontal (640 pixels) and the vertical (480 pixels) image size, respectively. $V_d(t,x)$ and $H_d(t,y)$ are the distribution functions representing the number of pixels with a temperature above T_{bcg} along every horizontal and vertical line of the field of view, thus representing the extension of the highest temperature areas in the two directions. This analysis enabled tracking of the front of the thermal anomaly in the vertical and horizontal directions by automatically picking the pixel coordinates where the distribution functions $V_d(t,x)$ and $H_d(t,y)$ increased (see Figure 4). Combining the information from the vertical and horizontal components, it was possible to calculate the apparent trajectory of the thermal anomaly. The thermal decomposition method was applied only in the vertical direction and, using the temperature threshold criteria, thermal imagery was reduced to a black-and-white image to enhance the thermal gradient of the hotter inner core of the plume, which in this case was 50°C. This hotter core region was assumed to be representative of the gas thrust portion of the plume and once all the images were converted, the mean position of the temperature contrast was used to define and track the change of plume height with time. The exit velocity, w, was computed assuming the energy balance of a fluid flowing out a reservoir through an opening, $w = \sqrt{2gh}$, where h is the height that the fluid reaches above the vent and g is the acceleration due to gravity. Therefore, the variations of the exit velocity within the 100–200 m s^{-1} range were calculated from the plume height derived by thermal image analysis of the eruptions at Etna. The maximum exit velocity that can be estimated is limited by the camera field of view (FOV).

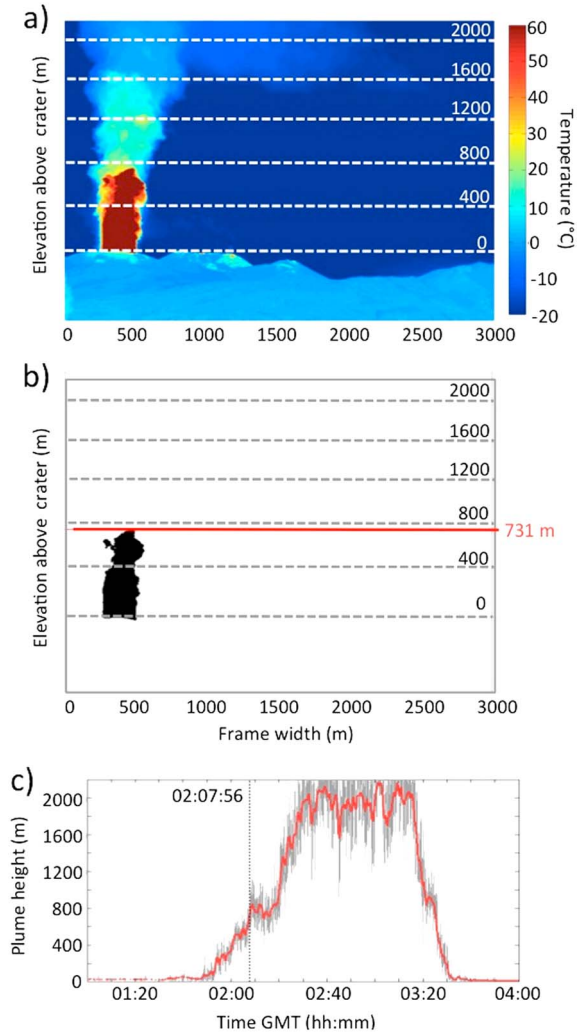

Figure 4. (a) The radiometric image acquired from the thermal camera on 3 December 2015 at 02:07:56 GMT. (b) The image mask isolating the plume gas thrust region. (c) The plume height evolution throughout the entire eruptive phase.

To overcome this limitation, alternative velocity measurements might be integrated in future work, i.e., the L band Doppler radar observations provided by the compact system, called VOLDORAD, installed on Mount Etna [*Donnadieu et al.*, 2016].

5. Data Set

5.1. Eruption Events

Mount Etna is one of the most active and well-studied basaltic volcanoes in the world, with more than 150 short-lived (from 20 min up to 10 h long) violent eruption episodes (named lava fountains) occurring in the past 25 years. These ash-rich events generate sustained plumes, whose top often exceeds 10 km height above the volcano vent. They lead to consequences for civil protection and local air traffic management.

After a few months of relative quiescence, four lava fountain episodes with related ash plume generation were observed between 3 and 5 December 2015.

On 2 December 2015 the infrasonic monitoring system documented a remarkable increase in activity starting around 18:00 GMT, whose oscillations, associated with Strombolian activity with a frequency of one event every 10 s, ranged between 1 and 3 Pa. In the following hours, the infrasonic activity underwent a continuous increase characterized by high oscillations (between 3 and 5 Pa), reaching a maximum between 02:00 and 03:20 GMT with a short lava fountain episode characterized by infrasonic pressure of 8 Pa. Subsequently,

Table 3. Main Information on the Considered Radar Systems

Acronym	Location	Latitude (deg)	Longitude (deg)	Height (m)	Tilts (deg)	Δr (km)	r_{max} (km)
DPX2	Reggio Calabria	38.07	15.65	22	1, 2, 3, 5, 6, 8 9.5, 11, 13.2 15.5, 18.3, 21.6, 90	0.1	80
DPX4	Catania	37.462	15.050	14	1,2 , 3, 5, 6, 8 9.5, 11, 13.2 15.5, 18.3, 21.6, 90	0.1	80
LAURO	Buccheri	37.116	14.836	980	0.5, 1.5, 2.5, 3.5, 4.5, 5.5, 7, 9, 11 13.5, 16, 90	0.15	200

the infrasonic activity sharply decreased, with oscillations of about 1.5 Pa associated with Strombolian activity with a frequency of one to two episodes per minute.

Starting on 00:30 GMT on 4 December 2015, the monitoring system registered a new increase of infrasonic activity, with oscillations exceeding 5 Pa with Strombolian activity repeated every 10 s.

At 08:16 GMT, a further increase of infrasonic oscillations was observed (up to 25 Pa) associated with lava fountains and a subsequent sustained plume. At 10:35 GMT, the infrasonic activity slightly decreased congruent with the reduction of the lava fountaining. A further increase of Strombolian activity with associated ash emission was registered between 20:00 and 22:30 GMT.

At 13:04 GMT on 5 December 2015, an increase of infrasonic activity was the prelude to the final lava fountain episode examined here, with associated ash emission that lasted about 2 h, starting at 14:47 GMT.

5.2. Radar Observations

The Etna volcano is monitored by three operational dual-polarization weather radars managed by the Department of Civil Protection. Two of them are compact systems operating at X band (the wavelength λ is about 3 cm) inside the airports of Catania (Sicily, Italy) and Reggio Calabria (Calabria, Italy) named DPX4 and DPX2, respectively, and located at about 32 and 67 km from the volcano vent. The third is a C band system ($\lambda \approx 5$ cm) (named LAURO), located on Mount Lauro (Buccheri, Syracuse, Italy) about 72 km from the volcano vent. Every 10 min the radars perform volumetric scans lasting about 5 min. The radar coordinates and scan strategies are listed in Table 3.

The radar located in Catania is the most sensitive for near-source monitoring purposes because of its shorter wavelength and distance from the volcano vent. According to the sensitivity analysis carried out in [*Marzano et al.*, 2006b] on similar radar systems, fine ash could be detected by the C band radar only for relatively high concentrations.

In addition to the reflectivity factor and radial velocity, the systems considered here provide the following observables:

1. The differential reflectivity Z_{DR} defined as the ratio, expressed in decibels, of reflectivity factors at two orthogonal polarizations. This observable is sensitive to particle shape and orientation. For oblate spheroidal particles, like raindrops falling with the semimajor axis canting around the vertical axis of symmetry, it is expected to be positive (even larger than 4 dB for large drops), whereas for irregularly shaped particles subject to tumbling motion during fall, Z_{DR} is expected to vary around 0.
2. The correlation coefficient ρ_{HV} is defined as

$$\rho_{hv} = \frac{\int S_{vv}(D) S_{hh}^{*}(D) N(D) \mathrm{d}D}{\sqrt{\int \mid S_{hh} \mid^2 N(D) \mathrm{d}D} \sqrt{\int \mid S_{vv} \mid^2 N(D) \mathrm{d}D}} = \mid \rho_{hv} \mid e^{j\delta_{hv}} \tag{22}$$

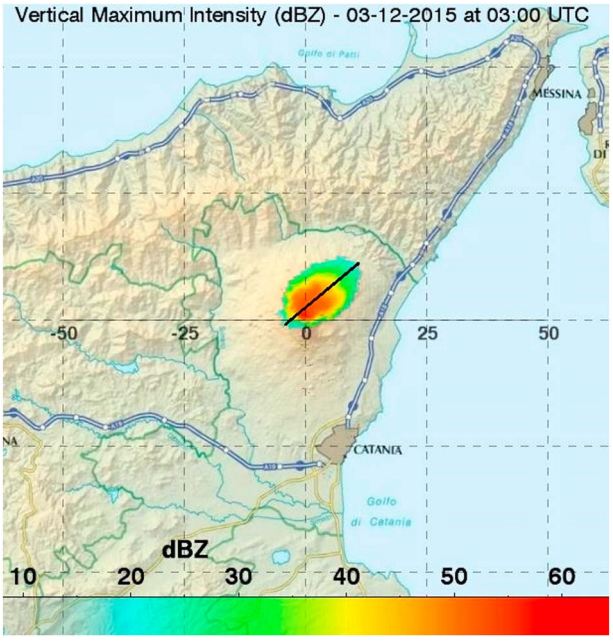

Figure 5. Map showing the maximum of reflectivity with respect to the vertical as observed by the X band radar system located in Catania (Sicily, Italy) on 3 December 2015 at 03:00 UTC. The black line identifies the vertical slice considered in Figure 6.

where S_{hh} and S_{vv} are the copolar backscattering matrix components at horizontal and vertical polarization, respectively. δ_{hv} (degrees) is the backscattering differential phase shift. The magnitude of ρ_{HV} is sensitive to the dispersion in particle eccentricities, canting angles, irregular shapes, and presence of heterogeneous targets.

3. The specific differential phase shift K_{DP} is defined as

$$K_{DP} = 10^{-3}\frac{180}{\pi}\lambda Re\int[f_{hh}(D) - f_{vv}(D)]N(D)\mathrm{d}D \tag{23}$$

where $f_{hh,vv}$ are the forward-scattering amplitudes at horizontal and vertical polarization and λ is the wavelength. K_{DP} is sensitive, on the one hand, to the target concentration and on the other hand to particle shape and orientation. Consequently, even high concentrations of spherical-like particles (or equivalent randomly falling irregularly shaped particles) provides low K_{DP} values.

The radar data were preliminarily processed (i.e., clutter removal and differential phase processing) according to the procedures proposed in *Vulpiani et al.* [2012] and *Vulpiani et al.* [2015]. Because it is closest, the DPX4 radar is clearly able to capture the larger portion of the ash plume in the proximity of the volcano. However, in the same area the bottom and top parts of the cloud might be better observed by DPX2 and LAURO due to the scan strategy used here, radar beam width, orography, and relative radar location. Regarding the DPX4, the lowest adopted antenna elevation that is potentially usable for observing the proximity of the vent is 6.0°, implying an observational height of about 100 m above the crater. However, due to the finite beam width, the lower part of the radar beam might intercept the ground. Consequently, the first totally unshielded tilt is 8.0°, which corresponds to an observational height of about 1.3 km above the volcano vent. As discussed in section 6.2, these observational characteristics entail an impact on the retrieval process.

6. Results

This section is dedicated to describing some features of the ash clouds observed in this study in terms of polarimetric radar signatures, then the retrieval of the MDR is discussed.

6.1. Ash Radar Signatures

To some extent, remote sensing measurements enable us to infer the underlying physical processes of the observed ash clouds [*Corradini et al.*, 2015]. More specifically, dual-polarization radar observables might add

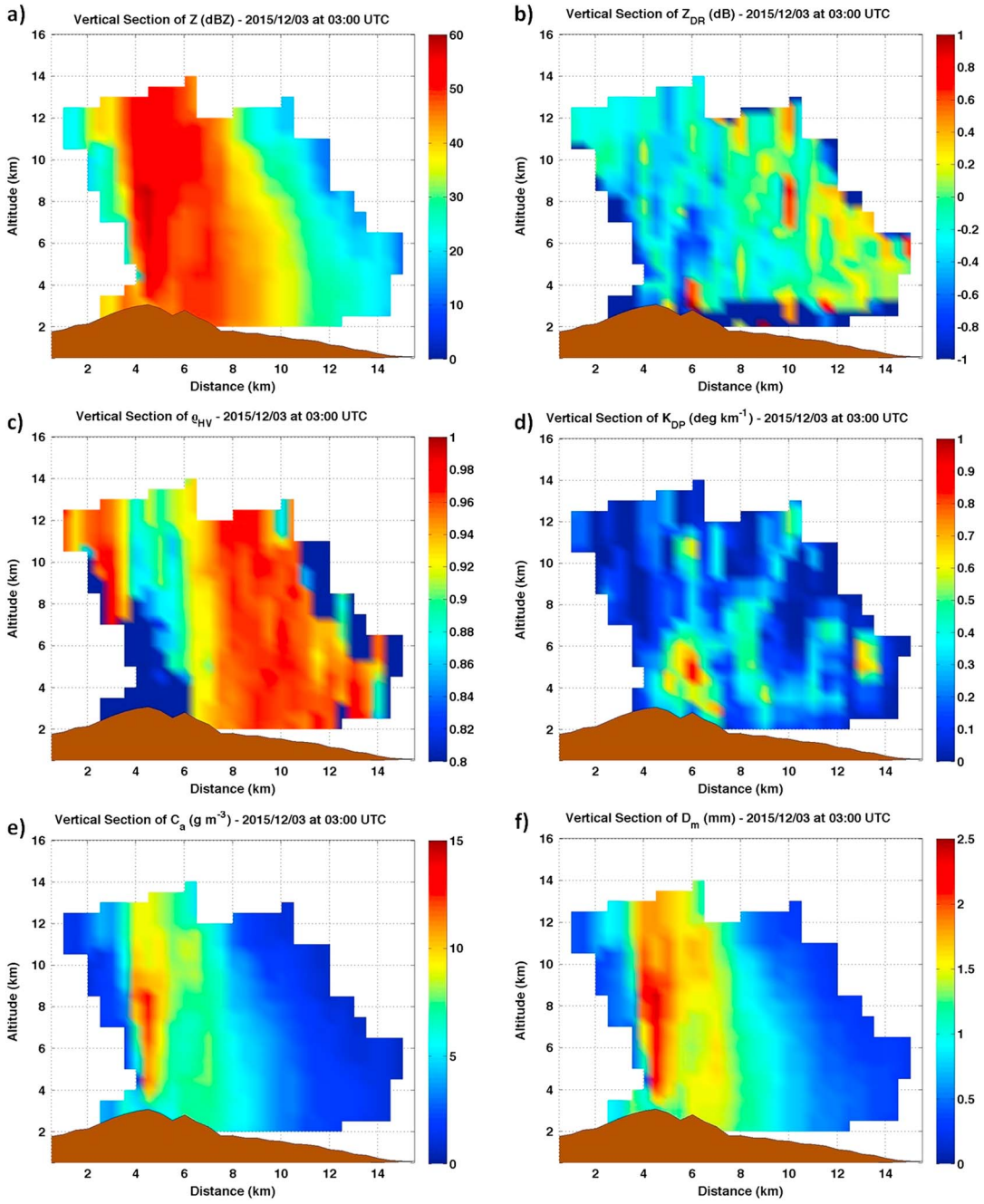

Figure 6. Vertical sections of the radar observables and related products along the direction depicted in Figure 5. (a) Z, (b) Z_{DR}, (c) ρ_{HV}, (d) K_{DP}, (e) C_a, and (f) D_m are shown.

valuable and unique information. By way of example, consider the analysis of the eruption that occurred on 3 December 2015 at 03:00 UTC. Figure 5 shows the vertical maximum of the echo intensity in terms of reflectivity (Z) as observed by the DPX4 system. This was the most intense phase of this eruption episode, with peaks of reflectivity exceeding 50 dBZ, symptomatic of high mass concentration. For the entire eruption, the cloud was not very widespread due to the relatively weak wind intensity; the radial velocity measured by the radars was generally found to be lower than ± 10 m s^{-1}. Figure 6 shows the vertical slices of the radar observables, ash concentration, and mean diameters taken at the direction depicted by the black line in Figure 5, roughly coincident with the major axis of the ash cloud. The reflectivity field shown in Figure 6a points out the intensity of the eruption episode characterized by peaks exceeding 55 dBZ up to 6 km above the volcano vent. The eruption column height reached at least 14 km asl—indeed, according to the observations collected by

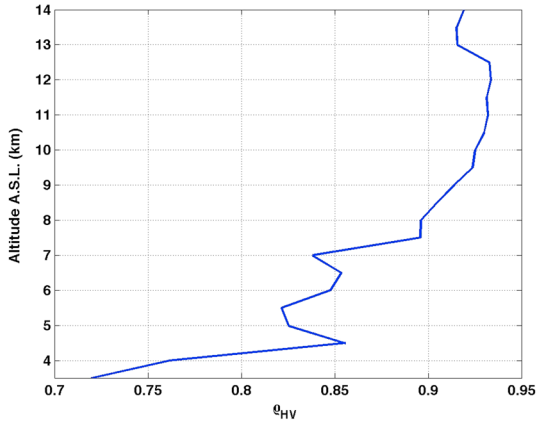

Figure 7. Vertical profile of the average copolar correlation coefficient as retrieved within the eruption column depicted in Figure 6.

the other radars discussed below, it exceeded 15 km (about 12 km above the volcano crater). Regarding the vertical section of Z_{DR}, it can be seen that it mostly ranges in the interval [−1, 1]. Correlating Z_{DR} with ρ_{HV}, it is found that $-0.5 \leq Z_{DR} \leq 0.5$ in 85% of the cases for $\rho_{HV} > 0.9$. This interval of Z_{DR} values is compatible with ash particles subject to tumbling motion. However, the correlation coefficient drops below 0.92 within the eruptive column, where Z_{DR} drops as well whereas Z enhances. This radar signature is likely related to the presence of a mixture of heterogeneous targets within the radar resolution volume caused by turbulence effects. It suggests the possibility of using ρ_{HV} jointly with Z to segregate the eruptive column from the rest of the ash cloud, e.g., $\rho_{HV} < 0.92$. Focusing on the eruptive column, it can be seen that the correlation coefficient gradually increases with altitude starting from 8 km at the highest, likely due to the transition from the convective to the umbrella region. The drop of ρ_{HV} in the far side of the column is likely related to a low signal-to-noise ratio (SNR) [*Bringi and Chandrasekar*, 2001], as it corresponds to low reflectivity values.

Concerning the specific differential phase, most of the values are found to be close to zero, symptomatic of a prevalence of spherical-like particles (i.e., spherical or irregularly shaped tumbling particles). The peak of K_{DP} at the side of the eruptive column might be attributed to the presence of water and ash aggregates. As expected, the estimated concentration pattern is congruent with that of reflectivity. A core of concentration exceeding 10 g m^{-3} can be noticed up to 10 km asl, mostly composed of small lapilli, as pointed out by the estimated mean diameters. Moreover, the size sorting with distance is quite clear from Figure 6f.

Focusing on the eruption column, Figure 7 shows the vertical profile of ρ_{HV}. A general increase of the correlation coefficient at increasing altitudes can be noted as a consequence of the reduction of turbulence motion. However, two local minima are found around 5.5 and 7 km. Interestingly, the lowest coincides with the top of the gas thrust region, as identified by the thermal camera. The higher might indicate the transition between the convective and umbrella regions.

These signatures might be related to the relative amplification of particle heterogeneity due to the reduction of size sorting depending on the vertical velocity. If this hypothesis is confirmed by further analysis, the ρ_{HV} signature could be considered to implement a self-consistent procedure for identifying the gas thrust region and retrieve the exit velocity.

6.2. Total Mass and MDR Estimate

This section focuses on the findings related to the retrieval of the total cloud mass and mass discharge rate for every eruption episode. Due to its relative distance, DPX4 is preferred for the estimate of the cloud mass, which is carried out on the native polar coordinates from the estimated volume of concentration ($M_{plume} = \int C_a(r, \phi, \theta) dr d\phi d\theta$). Additional information—e.g., the plume top—is retrieved by combining all three radar observations. The MDR is computed by first resampling the single-radar measurements in a Cartesian grid following a linear interpolation approach, then estimating the mass flux as described in section 3 using observations collected at the reference height of 4 km asl (about 700 m above the crater). Finally, a weighted average is applied to combine the single-radar estimates. To take into account the beam broadening, the weights were defined as the inverse of the radar distances from the volcano vent. The reference height was chosen based on the compromise between the need for considering near-source data

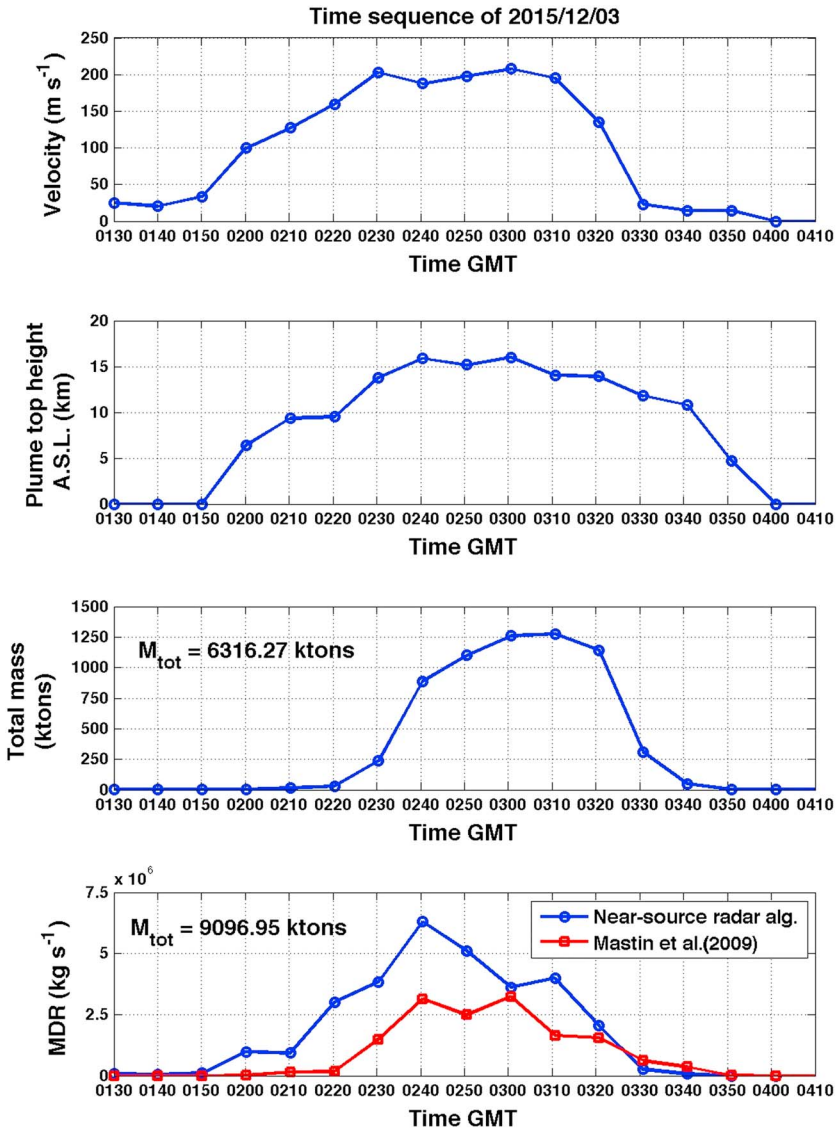

Figure 8. Estimated vertical velocity, plume height, total cloud mass, and MDR using C and X band radar observations on 3 December 2015 between 01:00 and 05:00 UTC.

and the need for avoiding ground clutter contamination, compatibly with the adopted scanning strategy, the distance from the volcano, and the radar beam broadening.

The time sequence of the maximum ash vertical speed within the gas thrust region, the cloud top height, the total cloud mass, and the MDR are shown in Figures 8–11 for the four eruption episodes. On 3 December 2015, a significant variation of the eruption velocity was registered between 02:00 and 03:20 GMT (see Figure 8). The most intense phase was observed between 02:30 and 03:10 GMT with speeds exceeding 200 m s^{-1}, while the plume top heights slightly exceeded 15 km asl (about 12 km above the volcano vent). However, due to the limited camera FOV, the maximum exit velocity was likely underestimated for this eruption episode. The time sequence of the plume mass, obtained by integrating the estimated three-dimensional plume concentration, is shown in Figure 8 (third panel).

The time integral provides an estimate of the total erupted mass for about $6.3 \cdot 10^9$ kg for this event. Due to the radar sensitivity, the discrete sampling strategy, the relative distance, and beam blockage induced by orography, a mass retrieval approach such as this is expected to underestimate the effective total erupted mass. Attenuation is another phenomenon affecting the estimate of any physical parameter. It depends on size, shape, concentration of the target, and the radar wavelength. In *Marzano et al.* [2006a], it was shown that

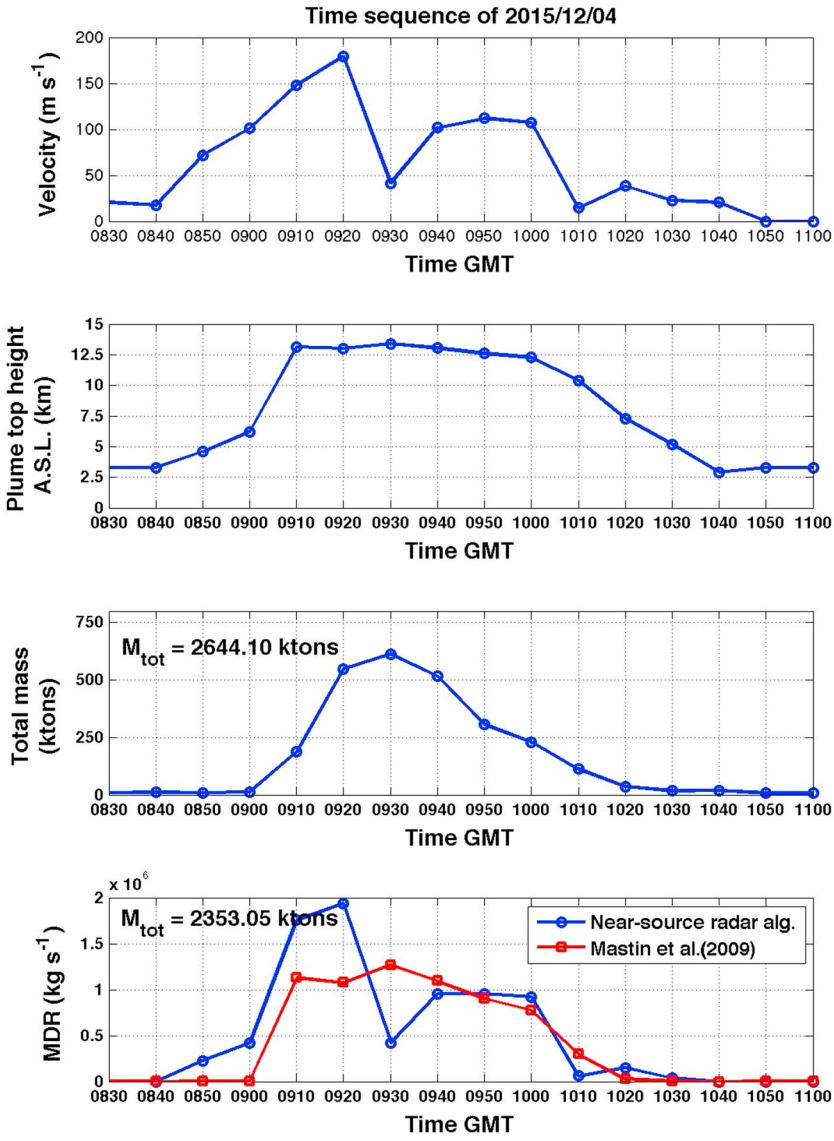

Figure 9. As in Figure 8 but for the eruption episode observed on 4 December 2015 between 08:30 and 11:00 UTC.

specific attenuation is expected to increase at increasing values of C_a and D_m. Indeed, it is of the order of 1 dB km^{-1} at X band for lapilli with $C_a = 10$ g m^{-3} (at C band it is much lower). However, the overall effect depends on the propagation path length. Consequently, attenuation is expected to affect the mass estimate derived by the volume integration of C_a more heavily than that obtained from the near-source computation of the MDR. Figure 8 (fourth panel) shows the time sequence of the MDR as estimated by the proposed near-source radar algorithm. The MDR retrieved from the plume top according to the methodology proposed by *Mastin et al.* [2009] is also shown for comparison. From the eruption onset to the end of the intense phase, around 03:20 GMT, there is at least a factor of 2 between the estimates obtained by the two approaches.

Generally speaking, the MDR obtained by the NSR algorithm is correlated with the exit velocity, as expected. However, this does not happen at 03:00 GMT. From the analysis of the single-radar estimates it is found that the LAURO radar retrieval drops down, lowering the weighted average. This discrepancy might be related to the delay between the nominal observation time, coincident with the beginning of the volume scan, and the time of the effective observation above the volcano vent that happens about 4 min later in case of the LAURO system due to the adopted inverse-elevation scan strategy (from the higher to the lower antenna tilts). The total mass estimated by integrating the MDR is about $9 \cdot 10^9$ kg.

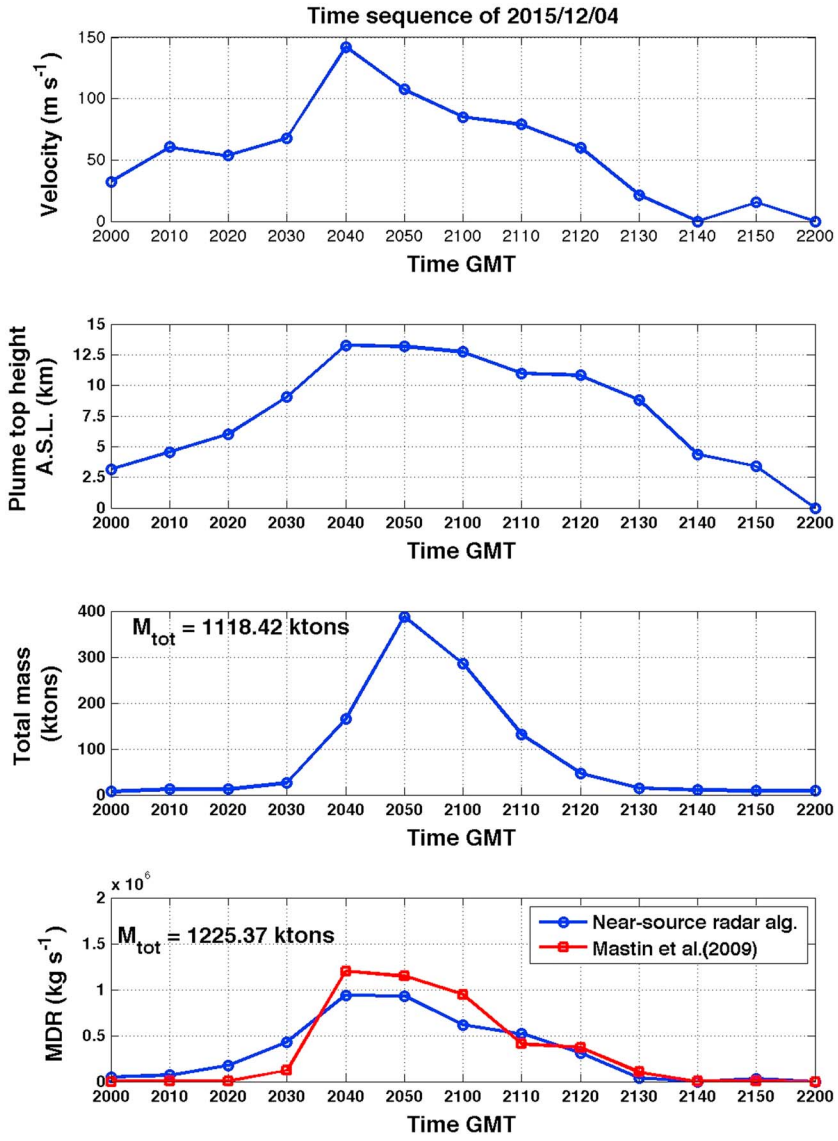

Figure 10. As in Figure 8 but for the eruption episode observed on 4 December 2015 between 20:00 and 22:00 UTC.

Two eruptions were observed on 4 December 2015. According to the time sequence shown on Figure 9, the onset of the first episode was around 08:50 GMT, the most intense phase was recorded around 09:20 GMT, and the eruption activity concluded around 10:10 GMT. The peak of the exit velocity, i.e., about 180 m s^{-1}, was estimated at 09:20 GMT, while the maximum retrieved plume top, measured about 10 min later, was about 13.4 km asl (about 10 km above the volcano vent). The total mass retrieved from the volume of plume concentration was about $2.6 \cdot 10^9$ kg, exceeding by about 12% that obtained from the derived MDR (see Figure 10, third and fourth panels). The MDR peak was about $2 \cdot 10^6$ kg s^{-1} as estimated at 09:20 GMT by the NSR algorithm. Around 09:30 GMT, the MDR estimated via the plume top height was clearly uncorrelated with the exit velocity as the buoyancy likely compensated the reduction of the intrinsic eruption rate. From 09:40 GMT to the end of the eruption, the two considered approaches provided comparable results. The second eruption episode that occurred on 4 December 2015 was characterized by a lower intensity in terms of the erupted mass. As shown in Figure 9, the peak was observed around 20:40 GMT, with an exit velocity of almost 150 m s^{-1}, while the plume top reached about 13.3 km. The corresponding MDR was $9.3 \cdot 10^5$ kg s^{-1} and $1.2 \cdot 10^6$ kg s^{-1}, as estimated using the NSR and *Mastin et al.* [2009] approaches, respectively. The total erupted mass was estimated to be about 122510^6 kg via the retrieved MDR—that is, approximately 9% higher than the value obtained from the plume concentration. The final episode, observed on 5 December 2015, lasted about 1 h. During the most intense phase, the exit velocity ranged between 150 m s^{-1} and about 60 m s^{-1}

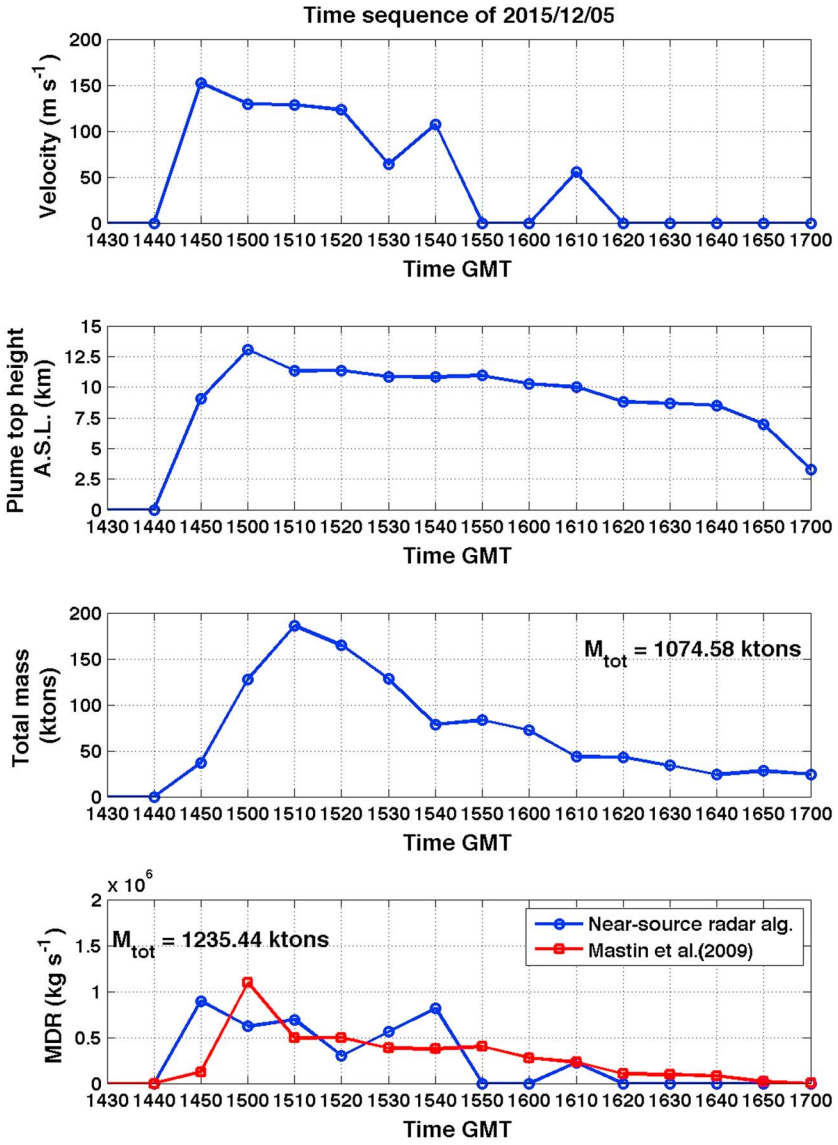

Figure 11. As in Figure 8 but for the eruption episode observed on 5 December 2015 between 14:00 and 17:00 UTC.

(see Figure 10, first panel). The MDR estimated through the NSR algorithm shows a peak of about 9.310^5 kg s^{-1} around 14:50 GMT. The plume top peak, about 13 km asl, was observed 10 min later. This implies a temporal shift of the mass eruption rate peak as retrieved from the plume top height. The total erupted mass derived by the mass discharge rate was about $1235 \cdot 10^6$ kg, about 13% higher than that obtained from the cloud concentration.

7. Conclusions

A novel methodology for estimating a volcano eruption's mass discharge rate based on the combination of radar and a thermal camera was presented here. It is based on the exact calculation of the mass flow using radar-derived ash concentration and particle diameter at the base of the eruption column and the exit velocity estimated by the thermal camera. The inversion algorithms adopted for deriving concentration and mean diameter are based on scattering simulations of polarimetric radar observables. The proposed procedure was tested on four Etna eruption episodes that occurred in December 2015 as observed by the available network of C and X band radar systems. The results are congruent with existing empirical methodologies deriving the mass eruption rate by the plume top height. The agreement between the total erupted mass derived by the retrieved MDR and the plume concentration can be considered as a self-consistent methodological

assessment. Interestingly, the analysis of the polarimetric radar observations allowed us to derive some features of the ash plume, including the size of the eruption column and the height of the gas thrust region. Future work will be devoted to a comparison with in situ observations and to the assimilation of radar-derived products in ash transport models. Furthermore, the use of near-source velocity measurements provided by the compact Doppler radar named VOLDORAD located on Mount Etna will be exploited to overcome the limitations of the thermal camera estimations.

Acknowledgments
All data used in this study are available at the Italian Department of Civil Protection repository. The scattering simulations were obtained using the T matrix code made available by the Goddard Institute for Space Studies (NASA) at http://www.giss.nasa.gov/staff/mmishchenko/t_matrix.html. The author G.V. is grateful to Emilio Guerriero for the optimization of Figures 3 and 5.

References

Adams, R., W. F. Perger, W. I. Rose, and A. Kostinski (1996), Measurements of the complex dielectric constant of volcanic ash from 4 to 19 GHz, *J. Geophys. Res.*, *101*(B4), 8175–8185.

Bringi, V. N., and V. Chandrasekar (2001), *Polarimetric Doppler Weather Radar*, p. 636, Cambridge Univ. Press, Cambridge, U. K.

Cadle, R. D., A. L. Lazrus, B. J. Huebert, L. E. Heidt, W. I. Rose, D. C. Woods, R. L. Chuan, R. E. Stoiber, D. B. Smith, and R. A. Zielinski (1979), Atmospheric implications of studies of Central American volcanic eruption clouds, *J. Geophys. Res.*, *84*, 6961–6968.

Casadeval, T. J. (1994), Volcanic ash and aviation safety, *U.S. Geol. Surv. Bull.*, *2047*, 450–469.

Corradini, S., et al. (2015), A multi-sensor approach for volcanic ash cloud retrievals and eruption characterization, *Remote Sens.*, *8*, 58, doi:10.3390/rs8010058.

Delle Donne, D., and M. Ripepe (2012), High-frame rate thermal imagery of Strombolian explosions: Implications for explosive and infrasonic source dynamics, *J. Geophys. Res.*, *117*, B09206, doi:10.1029/2011JB008987.

Donnadieu, F., P. Freville, C. Hervier, M. Coltelli, S. Scollo, M. Prestifilippo, S. Valade, S. Rivet, and P. Cacault (2016), Near-source Doppler radar monitoring of ash plumes at Etna, *J. Volcanol. Geotherm. Res.*, *312*, 26–39, doi:10.1016/j.jvolgeores.2016.01.009.

Harris, D. M., and W. I. Rose (1983), Estimating particle sizes, concentrations, and total mass of ash in volcanic clouds using weather radar, *J. Geophys. Res.*, *88*(C15), 10,969–10,983.

Maki, M., K. Iwanami, R. Misumi, R. J. Doviak, T. Wakayama, K. Hata, and S. Watanabe (2001), Observation of volcanic ashes with a 3-cm polarimetric radar, paper P5.13 presented at 30th International Conference on Radar Meteorology, American Meteorology Society, Munich, Germany, 18–24 Jul.

Marzano, F. S., G. Vulpiani, and W. I. Rose (2006a), Microphysical characterization of microwave radar reflectivity due to volcanic ash clouds, *IEEE Trans. Geosci. Remote Sens.*, *44*, 313–327.

Marzano, F. S., S. Barbieri, G. Vulpiani, and W. I. Rose (2006b), Volcanic ash cloud retrieval by ground-based microwave weather radar, *IEEE Trans. Geosci. Remote Sens.*, *44*, 3235–3246.

Marzano, F. S., S. Barbieri, E. Picciotti, and S. Karlsdóttir (2010a), Monitoring sub-glacial volcanic eruption using C-band radar imagery, *IEEE Trans. Geosci. Remote Sens.*, *48*(1), 403–414.

Marzano, F. S., S. Marchiotto, S. Barbieri, C. Textor, and D. Schneider (2010b), Model-based weather radar remote sensing of explosive volcanic ash eruption, *IEEE Trans. Geosci. Remote Sens.*, *48*, 3591–3607.

Marzano, F. S., E. Picciotti, G. Vulpiani, and M. Montopoli (2012), Synthetic signatures of volcanic ash cloud particles from X-band dual-polarization radar, *IEEE Trans. Geosci. Remote Sens.*, *50*, 193–211.

Marzano, F. S., E. Picciotti, M. Montopoli, and G. Vulpiani (2013), Inside volcanic clouds: Remote sensing of ash plumes using microwave weather radars, *Bull. Am. Meteorol. Soc.*, *94*, 1567–1586.

Mastin, L. G., et al. (2009), A multidisciplinary effort to assign realistic source parameters to models of volcanic ash-cloud transport and dispersion during eruptions, *J. Volcanol. Geotherm. Res.*, *186*, 10–21.

Mereu, L., F. S. Marzano, M. Montopoli, and C. Bonadonna (2015), Retrieval of tephra size spectra and mass flow rate from C-Band radar during the 2010 Eyjafjallajökull eruption, Iceland, *IEEE Trans. Geosci. Remote Sens.*, *3*, 5644–5660.

Mishchenko, M. I. (2000), Calculation of the amplitude matrix for a nonspherical particle in a fixed orientation, *Appl. Opt.*, *39*, 1026–1031.

Montopoli, M., G. Vulpiani, D. Cimini, E. Picciotti, and F. S. Marzano (2014), Interpretation of observed microwave signatures from ground dual polarization radar and space multi-frequency radiometer for the 2011 Grímsvötn volcanic eruption, *Atmos. Meas. Tech.*, *7*, 537–552, doi:10.5194/amt-7-537-2014.

Riley, C. M., W. I. Rose, and G. J. S. Bluth (2003), Quantitative shape measurements of distal volcanic ash, *J. Geophys. Res.*, *108*(B10), 2504, doi:10.1029/2001JB000818.

Rose, W. I., G. J. S. Bluth, and G. G. J. Ernst (2000), Integrating retrievals of volcanic cloud characteristics from satellite remote sensors—A summary, *Philos. Trans. R. Soc. A*, *358*, 1585–1606.

Steinberg, G. S., and J. L. Babenko (1978), Gas velocity and density determination by filming gas discharges, *J. Volcanol. Geotherm. Res.*, *3*, 89–98.

Vulpiani, G. (2010), *Remote Sensing of the Atmosphere by Ground-Based Radar: Advanced Techniques for Rainfall and Volcanic Ash Clouds Retrieval*, LAP LAMBERT Acad., Saarbrücken, Germany.

Vulpiani, G., M. Montopoli, E. Picciotti, and F. S. Marzan (2011), On the use of polarimetric X-band weather radar for volcanic ash clouds monitoring, paper presented at AMS Radar Conference, Pittsburgh, Pa., 26–30 Sep.

Vulpiani, G., M. Montopoli, L. Delli Passeri, A. G. Gioia, P. Giordano, and F. S. Marzano (2012), On the use of dual-polarized C-Band radar for operational rainfall retrieval in mountainous areas, *J. Appl. Meteorol. Climatol.*, *51*, 405–425.

Vulpiani, G., L. Baldini, and N. Roberto (2015), Characterization of Mediterranean hail-bearing storms using an operational polarimetric X-band radar, *Atmos. Meas. Tech.*, *8*, 4681–4698.